All-Blade-Coated Flexible Perovskite Solar Cells & Modules Processed in Air from a Sustainable Dimethyl sulfoxide (DMSO)-based Solvent System

Journal:	*Sustainable Energy & Fuels*
Manuscript ID	SE-ART-12-2022-001678.R1
Article Type:	Paper
Date Submitted by the Author:	06-Feb-2023
Complete List of Authors:	Jafarzadeh, Farshad; University of Rome Tor Vergata, Electronics engineering Castriotta, Luigi Angelo; University of Rome Tor Vergata, Dept. Electronic Engineering De Rossi, Francesca; University of Rome Tor Vergata, Dept. Electronic Engineering Ali, Jazib; University of Rome Tor Vergata, Dept. Electronic Engineering Di Giacomo, Francesco ; University of Rome Tor Vergata Di Carlo, Aldo; University of Rome Tor Vergata, Dept. Electronic Engineering matteocci, fabio; University of Rome Tor Vergata, Dept. Electronic Engineering Brunetti, Francesca; University of Rome Tor Vergata, Dept. Electronic Engineering

SCHOLARONE™
Manuscripts

All-Blade-Coated Flexible Perovskite Solar Cells & Modules Processed in Air from a Sustainable Dimethyl sulfoxide (DMSO)-based Solvent System

Farshad Jafarzadeh[a], Luigi Angelo Castriotta[a], Francesca De Rossi[a], Jazib Ali[a], Francesco Di Giacomo[a], Aldo Di Carlo[a,b], Fabio Matteocci[a], Francesca Brunetti[a,*]

[a]CHOSE (Centre for Hybrid and Organic Solar Energy), Department of Electronic Engineering, University of Rome Tor Vergata, Roma 00133, Italy
[b]CNR-ISM Istituto di Struttura della Materia, via del Fosso del Cavaliere 100, 00133 Rome, Italy

Abstract

Flexible Perovskite solar cells have been considered promising candidates for novel applications that require a high power-to-weight ratio. However, the scalable ambient air deposition of efficient devices remains a major challenge of this technology. In addition, toxic solvents are regularly used in perovskite layer deposition, which can damage the environment and endanger the safety of potential production lines. In this paper, we introduced sustainable flexible perovskite solar modules (flex-PSMs), in which all layers are deposited via a blade coating in ambient air without the usage of toxic solvents. Double-cation $Cs_{0.15}FA_{0.85}PbI_{3-x}Br_x$-based perovskite is blade coated in two steps as the absorber and the coating parameters are optimized. We found that proper drying of the first step is crucial to obtain high-quality perovskite films with the right phase of the perovskite. We improved the morphology and limited the voids in the perovskite layer by additive engineering and obtained 14% efficiency. Finally, 94 cm^2 modules are manufactured to demonstrate the scalability of the process.

Introduction

The organic-inorganic perovskite solar cells (PSCs) are an excellent choice for flexible devices owing to their high power conversion efficiency and low-temperature solution-processing fabrication techniques. Flexible PSCs (flex-PSCs) deliver a high power-to-weight ratio, are low cost, and are environmentally friendly[1–5]. Flexibility and low weight make them adaptable to various surfaces and enable broad applications such as tandem photovoltaics[6,7], photovoltaics in space[8], building-integrated photovoltaics[9,10], wearable electronics11 and the Internet of Things (IoT)[11,12]. Recently, flex-PSCs have shown great progress, reaching over 22% power conversion efficiency (PCE) [13]. However, record-breaking flex-PSCs are made by spin-coating with a small active area below 1 cm^2 and under the N_2 atmosphere. The performance of these solar cells decreases when deposited on large scale due to transparent conductive oxide (TCO) resistivity and decreased uniformity of the film. For instance, PCE decreased from 20% to 15.5% for flex-PSCs by transferring

spin-coated small cells to 100 cm^2 blade-coated modules fabricated in a controlled environment [14]. Moving to ambient air fabrication further decreases the performance, as humidity adversely affects the morphology of the perovskite film by changing growth kinetics [15]. Hence, the deposition of a large-area flexible perovskite layer in ambient air is one of the main challenges in flex-PSCs.

Among large-area deposition techniques, blade coating is one of the most widely used solution-processable methods for PSCs [16,17]. It is a high-throughput deposition method that requires simple equipment and is transferrable to roll-to-roll fabrication with slight modifications. Blade coating of the perovskite layer in ambient environments is only possible by means of hot casting, gas quenching, vacuum extraction, or a combination of these methods to prevent moisture spreading over the perovskite phase [18]. Exposure of the intermediate phase (i.e., PbI$_2$-DMSO-MAI) to moisture results in poor quality perovskite film [19]. Yang et al. showed dense and dark brown perovskite layers, blade coated at 15-25% RH from a DMF-based solvent system, turned into nonuniform films with a grayish color at 60-70% RH and PCE dropped from 10.44% to 0.35%[20]. An effective strategy is the two-step deposition of perovskite films, which prevents the formation of the intermediate phase and allows the ambient deposition of perovskite. Two-step deposition of the perovskite layer is a common technique for the spin coating method: First, the PbI$_2$ layer is deposited on the substrate and converted to perovskite by a second deposition or immersion in the organic halide salt solutions. Controlling the crystallization dynamics is simpler than in one-step deposition[21]. In this way, a high-quality PbI$_2$ film is formed, and the conversion to perovskite occurs thereafter. Matteocci et al. fabricated large-area PSCs in ambient conditions through the coating of the blade of PbI$_2$ layers and immersion in MAI solution in isopropyl alcohol (IPA) [22]. They added MAI to the PbI$_2$ ink to slow down crystallization and avoid large lead iodide grains. Castriotta et al. showed that it is also possible to blade coat double-cation perovskite using two-step deposition in ambient air with the help of gas quenching and additive engineering[23]. The effect of moisture was alleviated by adding FAI and CsI to the PbI$_2$ ink. In addition, the double cation perovskites endured 1000 hours of light soaking.

A major obstacle to the large-area processing of PSCs is the usage of toxic solvents. For example, studies on the perovskite layer blade coating use primarily toxic solvent systems that include dimethylformamide (DMF) [22,24–26], 2-methoxyethanol (2-ME) [23,27,28] or N-Methyl-2-pyrrolidone (NMP) [23,27,28]. Although solution processability is the main advantage of the PSCs and reduces fabrication complexity and cost, with current solvent systems, transferring the process to a large area becomes an environmental issue. The use of toxic solvents for mass production releases a massive volume of solvents and pollutes the atmosphere. The most commonly used solvent in PSCs is dimethyl formamide (DMF) which the European Union will prohibit the use of as a solvent from 2023[29]. Therefore, the elimination of toxic solvents is essential for the commercialization of PSCs. Among common polar aprotic perovskite solvents, DMSO has the lowest environmental and human health impact based on a life cycle assessment (LCA)[30]. Moreover, the wastewater of DMSO can be efficiently managed since it is decomposable to methanesulfonic acid using ultraviolet or ozone-based oxidation[31].

DMSO has good solubility and coordination capability of perovskite precursor salts. The tendency of solvents to donate electron pairs, donor number, was introduced by Gutmann[32]. Hamil et al. noticed a correlation between donor number and coordinating ability of perovskite precursors for solvents and the solubility of perovskite precursor salt(s) [33]. Consequently, higher DN results in better solubility and more control over the crystallization. Thus, low DN solvents such as acetonitrile (ACN), gamma-butyrolactone (GBL) and 2-Methoxyethanol (2-ME) can only dissolve

lead halides in the presence of organic salts[34]. DMSO has the highest DN among these solvents, and it can dissolve PbI_2 in the presence of different halide salts and can be used to deposit compositions of MA-based, FA-based, Cs-based, and mixed cation perovskite[35,36]. DMSO is mainly used as co-solvent in perovskite deposition and the development of efficient PSCs based on DMSO is encouraged[37]. However, DMSO is a nonvolatile solvent with a high boiling point (189 °C) and a low vapor pressure (0.6 mm Hg at 25°C). External force to extract solvent from the wet film is required to deposit the perovskite layer from a perovskite precursor solution based on a DMSO containing solvent system.

Studies that deposited perovskite in ambient air, using a mixture of DMSO with DMF or GBL, used relatively high blading temperature (> 150 °C) to overcome the adverse effect of humidity during perovskite phase formation[38–40]. In addition, high temperature is required to prevent DMSO trapping in the perovskite film[41]. Therefore, there is lack of low-temperature processed DMSO-based blade coated perovskite layer in the literature.

In this work, we used a two-step blade coating method to deposit a perovskite layer at low temperature in ambient air using DMSO only as the solvent for the first step and isopropyl alcohol (IPA) for the second step. Low-temperature deposition of DMSO-based ink is introduced for the first time to apply on flexible substrates. Previous works on single-step deposition of DMSO-based perovskite solution, using the blade coating technique required high substrate temperature (150 °C) or high annealing temperature (170 °C) [36,42]. In addition, the previously reported devices were fabricated under a nitrogen atmosphere. With the help of additive engineering and optimized drying of the wet film with high-flow gas quenching, we obtained a smooth film of $Cs_{0.15}FA_{0.85}PbI_{3-x}Br_x$ perovskite on a large coating area (94 cm^2). We fabricated flexible perovskite solar cells with a planar N-I-P device architecture of PET/ ITO/ SnO_2/ $Cs_{0.15}FA_{0.85}PbI_{3-x}Br_x$ / PTAA/ Au in ambient air with a relative humidity of 30-35%. Solar cells are blade coated on large substrates (5×7 cm^2) but measured on small scale with 0.09 cm^2 active area, and the champion device achieved 14.08% PCE.

Experimental Methods

Materials

Dimethyl sulfoxide (DMSO) ≥ 99.99%, toluene 99.5%, l-alpha-phosphatidylcholine (LP) ≥ 99%, tert-butylpyridine (TBP) 96%, Li bis(trifluoromethanesulfonyl)imide 99.95%, acetonitrile 99.8%, and 2-propanol 99.5% were purchased from Sigma-Aldrich. Lead (II) iodide (PbI_2) for perovskite precursor 99.99% and cesium iodide (CsI) ≥ 99.0% were purchased from Tokyo Chemical Industry (TCI). Formamidinium iodide (FAI) ≥ 99.99% and formamidinium bromide (FABr) ≥ 99.99% were purchased from Greatcell Solar Materials. Tin (IV) oxide (SnO_2) colloidal nanoparticles in water 15% wt. was purchased from Alpha-Aesar. Poly[bis(4-phenyl)(2,4,6-trimethylphenyl)amine] (PTAA) 105 kDa was purchased form Solaris Chem.

Solar cell Fabrication

Figure 1 depicts the fabrication procedures of flexible perovskite solar cells in ambient air (T ≈ 20-25 ˚ C and RH ≈ 30-35%). To use flexible substrates for the sheet-to-sheet blade coating method, 7×5 cm^2 pieces of PET/ITO are laminated on glass. Lamination prevents the substrate from dangling during deposition and helps to fix the substrate on the blade coater. 1 cm from the top and bottom of the substrates excluded due to the non-uniformity of the beginning and end of the blade-coated film. An aqueous colloidal dispersion of tin oxide nanoparticles (15 % wt., Alfa Aesar) was diluted to 2.5% wt. and blade coated on PET/ITO substrate with the speed of 15 mm/s followed by annealing at 100 ˚ C for 15 minutes. PbI_2-$(FAI)_{0.3}$-$(CsI)_{0.15}$ 1M solution in DMSO with

0.25 mg/ml LP additive was blade coated with 5 mm/s speed and 40 μm gap height of the blade. The hotplate temperature was set to 60 ˚ C while an air-knife with the flow of 120 L/min with 90˚ incident angle and distance of 50 mm was blowing from the top. The air-knife nuzzle had the length of 25 cm and can be seen in the **Figure S1 b**. Then FAI/FABr 30 mg/7.5 mg in IPA is coated with a speed of 2 mm / s and a hotplate temperature of 60 C followed by IR treatment using two Helios Quartz IR lamps for 2 minutes. The orange film turned dark brown after annealing at 130 ° C for 45 minutes. The PTAA layer (12 mg/ml in toluene) spin coated at 1500 rpm for 35 s. 5 μL of TBP and 10 μL of Li-TFSI salt (170 μm/ml in ACN) were added to the PTAA ink. An Au electrode with 100 nm thickness was deposited by thermal evaporation. The substrates were cut into four 2.5 × 2.5 cm^2 substrates (each hosting four cells).

Modules Fabrication

Modules were manufactured on 7×7 cm^2 and 13×13 cm^2 substrates by blade coating of all layers (ETL, absorber and HTL). The mini modules had a total module area of 5×5 cm^2 consisting of 7 cells with a cell width of 5 mm and a width of 0.3 mm for interconnections. The total active area was 18.55 cm2, excluding the dead area. The larger modules layout consisted of 17 series connected cells with a height of 9.7 cm and a width of 0.5 cm, for a total active and aperture areas of 82.45 cm^2 and 94.09 cm^2 (9.7×9.7 cm^2) respectively. 13×13 cm^2 substrates were secured to the blade coater plate using a vacuum holder. The ETL and perovskite were deposited as mentioned in the previous section. PTAA (12 mg/ml in toluene) was blade coated at 40 mm/s speed while the blading gap was set to 100 μm. P1-P2-P3 laser ablations [43] were obtained through a UV Nd:YVO$_4$ laser beam (355 nm wavelength, 2 μm spot size); more specifically, P1: 1.35 μJ pulse energy, 1600 pulses/mm; P2: 0.35 μJ pulse energy, 350 pulses/mm; P3: 0.5 μJ pulse energy, 250 pulses/mm.

Characterization

All solar cells were deposited in a large area (7×5 cm^2) and measured under standard AM1.5 conditions after cutting to a small area (2.5×2.5 cm^2) using a class A solar simulator (ABET Sun 2000) masked with an aperture area of 0.09 cm^2. A Si reference cell (RR226-O, RERA Solutions) was used for calibration of the sun simulator. The external quantum efficiency (EQE) spectra were measured using a measurement system by Arkeo–Cicci research s.r.l. The scanning electron microscopy images of thin films were captured by TESCAN MIRA microscope. Optical images were obtained by Olympus Lext OLS 3100 confocal microscope. Confocal microscopy provides a topographic map by transforming a series of optical sections taken from the surface that can be used to measure surface roughness[44].   Surface roughness measurement from this technique is proved to be comparable to stylus instruments[45]. Gwyddion software was used to calculate surface roughness from confocal microscopy results[46]. Rigaku SmartLab SE was used to measure X-ray diffraction patterns.
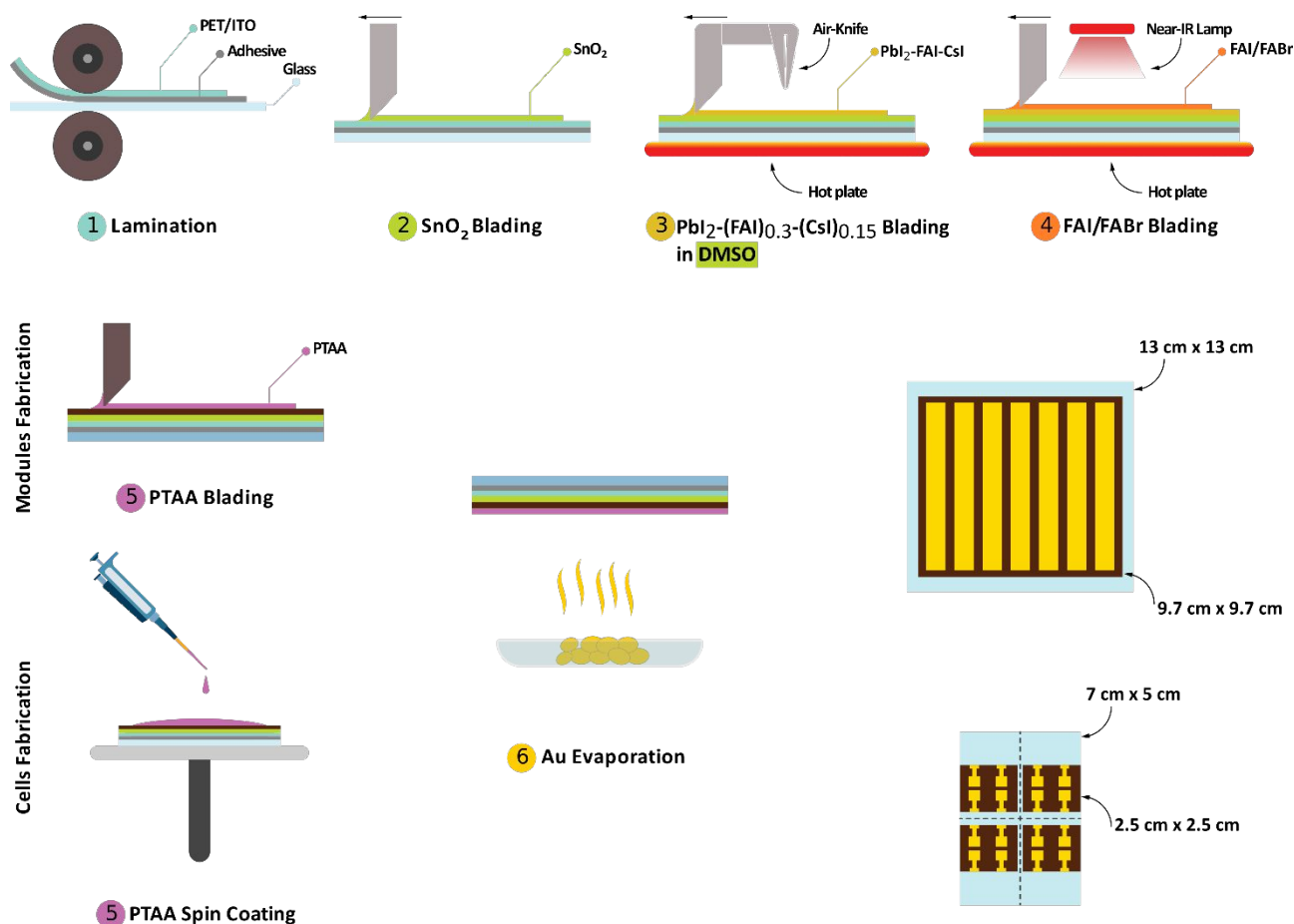
Figure 1. Fabrication process flow of the flexible perovskite cell and modules.

Results and Discussion

Table 1 summarizes boiling point, Gutmann's donor number (DN), and environment, health, and safety (EHS) scores of common solvents for perovskite layer. The EHS scores were adopted from the CHEM21 study on a scale of 1 to 10 and a three-color code (green, yellow, and red) [47]. The safety score mainly reflects the flammability of the solvents, the environment score is related to environmental issues, and the health scores reflect the occupation hazard, which is crucial for production lines. It is obvious from Table 1 that DMF, NMP, and 2-ME fail the health criteria and are classified as hazardous solvents. The non-hazardous solvents on the list are DMSO, ACN, and GBL but the last two have some limitations. ACN is not toxic, but the additives and cosolvents that are normally used with it are considered toxic. Most studies address the solubility issue of ACN by adding methylamine gas which is hazardous and flamable[47]. On the other hand, GBL has high environmental impacts and a high boiling point above 200 ˚C which would be inconvenient for flexible substrates[48]. Hence, among commonly used solvents, DMSO is an attractive option due to its ability to dissolve perovskite precursors (high DN) and its low environmental and toxicological concerns. Therefore, we selected DMSO as the main solvent for the perovskite layer. The perovskite layer was deposited by a two-step blade coating method that utilized a DMSO-only solvent system for the first step and IPA for the second step. First, PbI_2-$(FAI)_{0.3}$-$(CsI)_{0.15}$ is deposited and then it is converted to the perovskite phase by blade coating of an FAI/FABr solution in IPA. Adding a non-stoichiometric amount of organic halide salts to the first step solution has been shown to enhance the porosity of the PbI_2-$(FAI)_{0.3}$-$(CsI)_{0.15}$ layer which helps the conversion process to the perovskite phase during the second step [22]. Furthermore, because of the low solubility of cesium halide salts in IPA, CsI was added to the first step. The presence of CsI and FAI in PbI_2 ink affects the crystal growth of the layer as nucleation agents and facilitates

heterogeneous nucleation by reducing the free energy barrier [49]. Furthermore, the PbI_2-FAI-CsI complex may assist in the complete conversion of the film to the perovskite phase during step second [50].

Table 1. A list of common solvents in the perovskite layer blade coating [22–25,27,28,51–55] with their boiling points, donor numbers [33,56,57], and EHS scores based on CHEM21 study[47].

Solvent	Boiling Point (° C)	Donor Number (kcal/mol)	CHEM21 SCORE			Usage
			Environment	Health	Safety	
N, N-Dimethylformamide (DMF)	153	26.6	5	9	3	Solvent [22,24,25]
N-Methyl-2-pyrrolidone (NMP)	202	27.3	7	9	1	Solvent[23,27,28]
2-Methoxyethanol (2-ME)	124	19.7	3	9	3	Solvent[54,55,58]
Gamma butyrolactone (GBL)	204	18.0	7	4	1	Solvent[52,53]
Acetonitrile (ACN)	82	14.1	3	3	4	Solvent[51]
Methylamine	-6	N/A	7	5	7	Solvent Additive[51]
Dimethyl sulfoxide (DMSO)	189	29.8	5	1	1	**Solvent (This Study)**

To adopt an all-DMSO solvent system for the first step of deposition, we attempted to optimize the solvent evaporation rate by tuning substrate temperature and gas quenching parameters. The evaporation rate alters the degree of supersaturation which affects the nucleation rate [18,25]. We observed that depending on the blading parameters, ink drying was divided into four categories of ambient drying, incomplete drying, optimized dying, and overdying, which are shown in **Figure 2**. As expected, blade coating at room temperature without an air knife for gas quenching resulted in the formation of a wet film that required more than 3 minutes to naturally dry after blade coating. Slow evaporation of the DMSO leads to low supersaturation and allows crystals to grow faster than the nucleation rate. In this situation, the supersaturation is not enough for an appropriate nucleation rate. The long drying time allowed the formation of a noncontinuous film and large needle-like PbI_2 crystals visible to the naked eye. We name this ambient drying because there is no external force to drive solvent evaporation and the drying occurs in the ambient environment.

The opposite extreme of ambient drying is the over-drying situation. Upon increasing the supersaturation rate by hot casting (100˚ C substrate temperature), hot air knife (100 C) or high-pressure air knife (flow rate of 150 L/min), we observed phase separation in the PbI_2 -$(FAI)_{0.3}$-$(CsI)_{0.15}$film with dark perovskite regions appearing occasionally on the yellow PbI_2 film (**Figure S2 b**). Although in the single-step perovskite deposition, a very high degree of supersaturation is beneficial and assists the direct conversion of the precursors to the perovskite phase [19]. It normally requires high blading temperatures around 150˚ C to deposit high-quality perovskite films in ambient air [38,39] which is not recommended for flexible substrates. Therefore, direct conversion of perovskite precursors in ambient conditions is not possible for flexible substrates. In the two-step method, the CsI/FAI are present to retard the PbI_2 crystallization. However, the high supersaturation in our PbI_2-$(FAI)_{0.3}$-$(CsI)_{0.15}$ ink resulted in the reaction of CsI/FAI salts with the lead iodide and the formation of the perovskite phase. After the second step deposition, this phase separation results in the formation of islands in the perovskite film **(Figure S3 f and j)**.
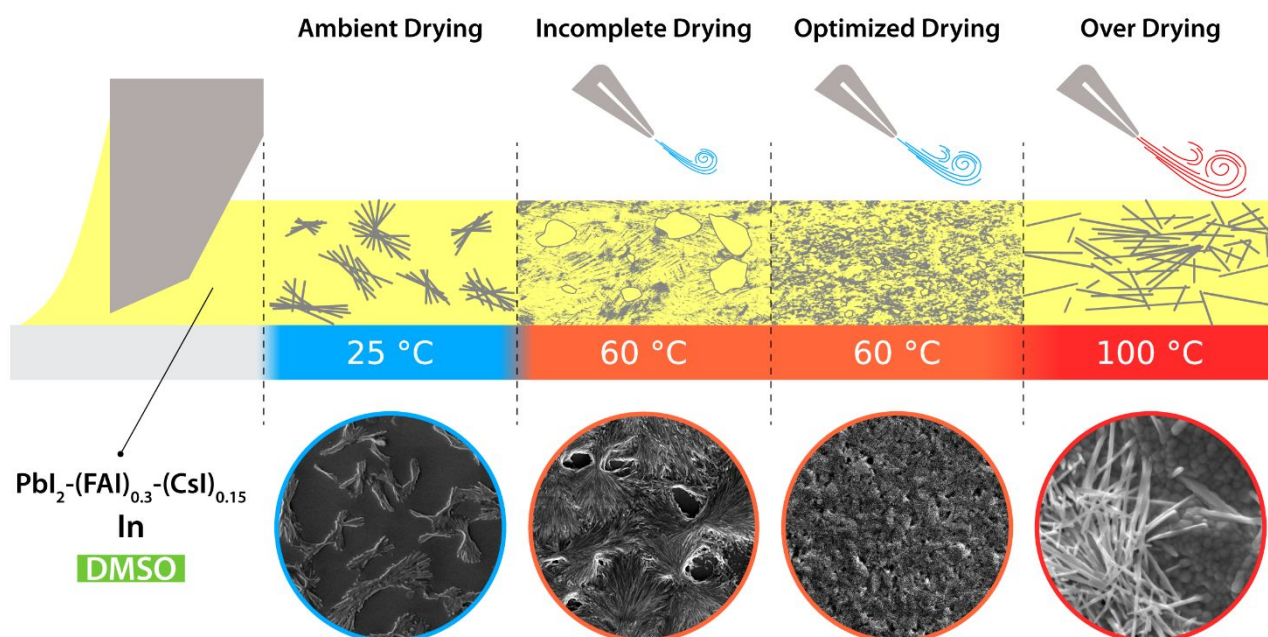
Figure 2. *The optimization of the drying of the DMSO-based PbI$_2$-(FAI)$_{0.3}$-(CsI)$_{0.15}$ ink by variation of substrate temperature, air-knife flow rate, and air-knife temperature and the corresponding SEM images.*

A trade-off is found when the substrate and air knife are settled at a temperature of 60 ° C using a flow rate of 120 L/min. The film is partially dried after blading and the drying is completed after approximately 30 s. Therefore, we name it incomplete drying. The mild temperature (60 °C) increased the nucleation rate and decreased the crystallization time, leading to smaller grains and a more uniform yellow film. However, due to incomplete drying after blading, the SEM image in **Figure 2** indicates a PbI$_2$-(FAI)$_{0.3}$-(CsI)$_{0.15}$ layer with micron-scale voids that could be the result of the moisture attack [40]. To prevent the incomplete drying of the film, we decreased the blading speed from 10 mm/s to 5 mm/s. As a result, the total volume of air striking the wet film doubles without increasing the air pressure and without exceeding the supersaturation level that leads to overdying. The wet film dried instantaneously after the blading / drying deposition steps. A smooth PbI$_2$-(FAI)$_{0.3}$-(CsI)$_{0.15}$ film is deposited without hot casting or hot gas quenching. **Figures S2 b and c** illustrate the smoothness of the film compared to incomplete drying. We name this optimized drying because the drying step occurs after applying the airflow at optimized flow rates without exposing the wet film to the ambient moisture.

As is evident from the SEM images in **Figure S3,** the optimized drying of the PbI$_2$-(FAI)$_{0.3}$-(CsI)$_{0.15}$ film is more uniform and the large voids disappeared. However, there are pores with 150-200 nm diameter. This porosity could be helpful in the conversion of PbI$_2$ to the perovskite phase. After the second step deposition (FAI/FABr), the yellow film is turned into a dark orange and consequently dark brown after the annealing and a smooth perovskite layer is formed.
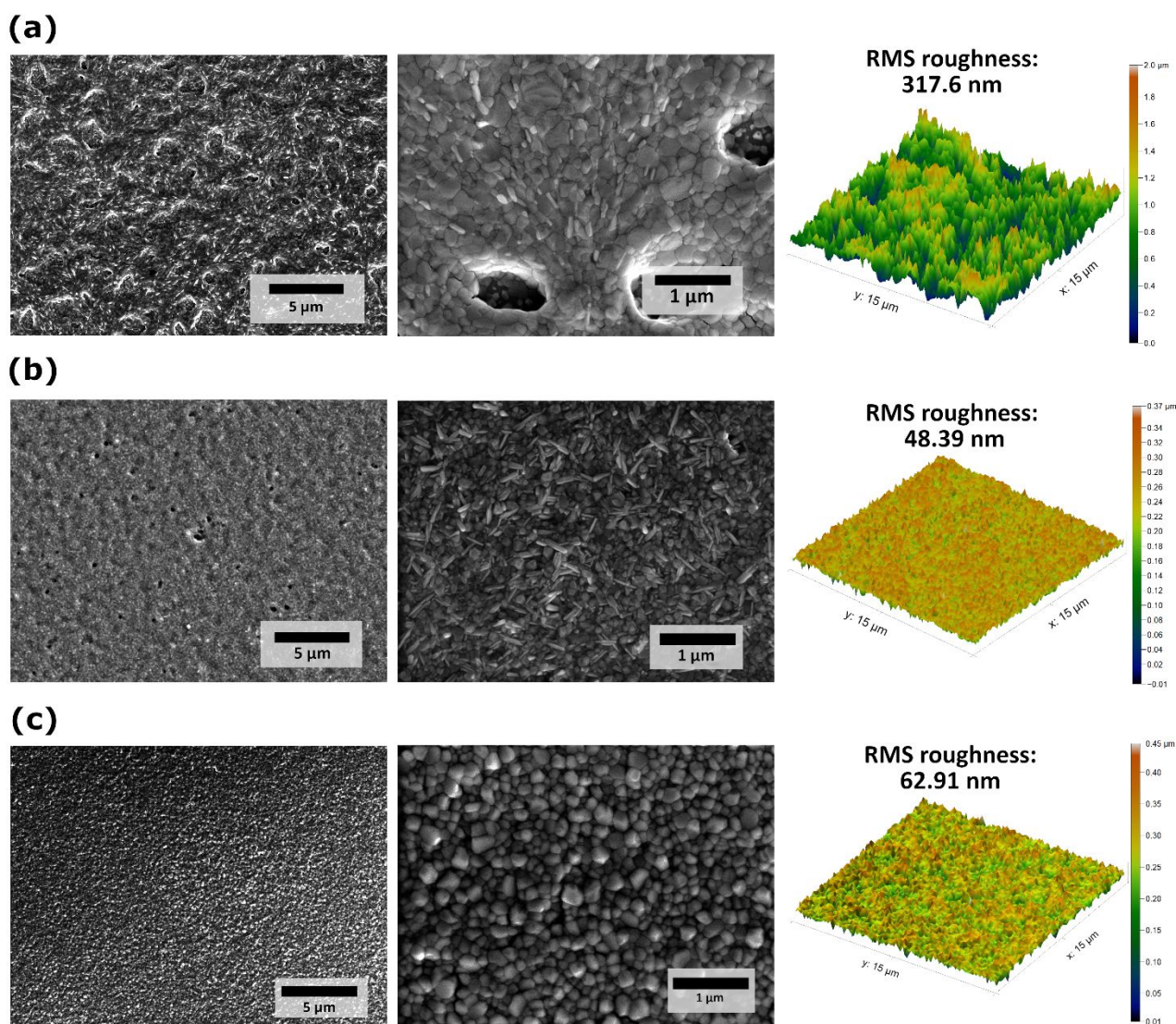
(a)

(b)

(c)

Figure 3. SEM and confocal 3D microscopy images of the perovskite layer deposited in incomplete drying conditions (a), optimized drying (b), and optimized drying + LP additive (c).

Figure 3 a shows SEM images and 3D projection of the confocal microscopy of the perovskite film when the first layer is incompletely dried. Microscale voids remained after conversion to the perovskite layer, and some crystals are visible on top of the film suspected to be needle-like PbI_2 crystals.

Using optimized drying, as evident from the SEM images in **Figure S3**, the PbI_2-$(FAI)_{0.3}$-$(CsI)_{0.15}$ film is more uniform, and the large voids shrink to a smaller size (150-200 nm). This porosity could be helpful in the conversion of PbI_2 to the perovskite phase. However, **Figure 3 b** indicates that the pores remained even after conversion to the perovskite phase. We modified the crystallization of the perovskite by adding L-α-phosphatidylcholine (LP) to the PbI_2-$(FAI)_{0.3}$-$(CsI)_{0.15}$ ink. LP is a naturally occurring amphoteric zwitterionic surfactant derived from egg yolk, used as an additive in the single-step blade coating of the perovskite layer to reduce surface tension and passivate charge traps [36,59–62]. We investigated the effect of this additive in two-step blade coating of the perovskite for the first time by adding this surfactant to the PbI_2-$(FAI)_{0.3}$-$(CsI)_{0.15}$ ink. The morphology of the PbI_2-$(FAI)_{0.3}$-$(CsI)_{0.15}$ film remained unchanged by addition of the LP as shown in **Figures S3 a-c**. However, it improved the morphology, increased the grain size, and eliminated the voids after conversion to the perovskite phase (**Figure 3 c**). Most likely, the additive slows down the crystallization of the perovskite phase and facilitates the growth of crystals. Additionally, small

needle-like crystals (PbI_2) are not visible in the LP-added sample, suggesting that it helps to convert PbI_2 to the perovskite phase in ambient air and improves film quality. LP did not alter the crystallization of the first step, and the voids remained identical. But after the second step and annealing, the voids in the LP containing the samples. This is more visible in the SEM images which depicts PbI_2-$(FAI)_{0.3}$-$(CsI)_{0.15}$ layer (**Figure S4 a-c**) and their corresponding perovskite layer (**Figure S4 d-j**) w/o and with LP additive. We measured the roughness of the perovskite film deposited in incomplete drying and optimized drying + LP additive by confocal microscopy. The root mean square (RMS) roughness decreased significantly in optimized drying compared to incomplete drying dropping from 317.16 nm to 48.39 nm. The addition of LP enlarged the grain size as shown in **Figure 3 c,** and consequently the roughness increased to 62.91 nm.
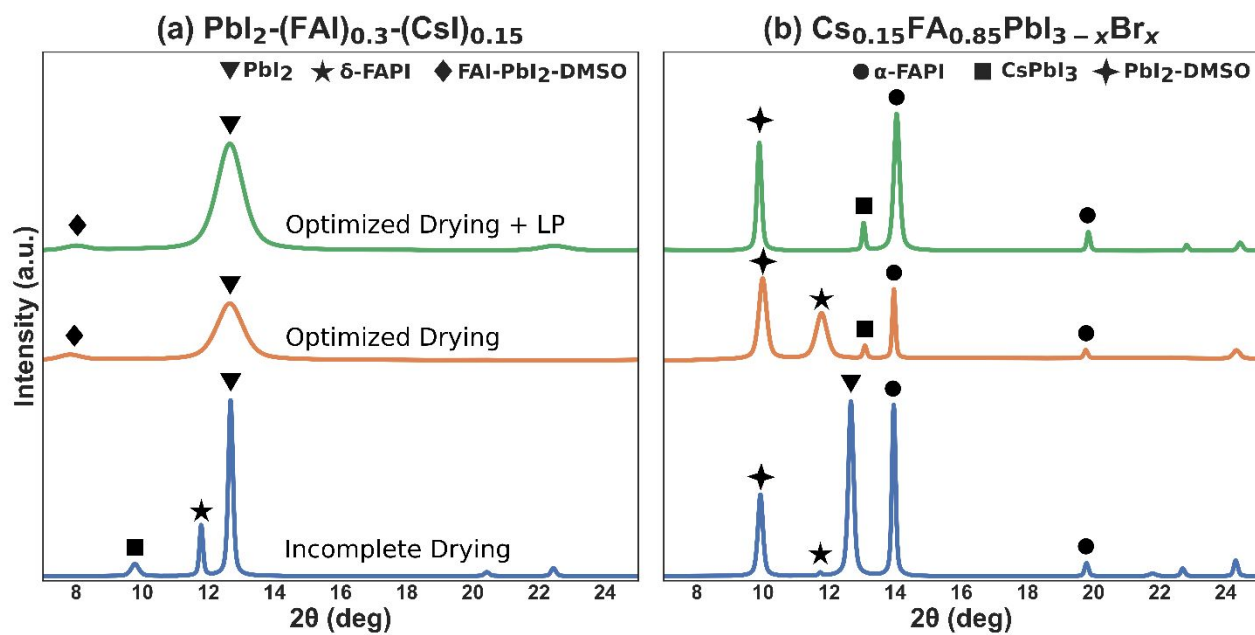

Figure 4. X-ray diffraction pattern of (a) PbI_2-$(FAI)_{0.3}$-$(CsI)_{0.15}$ after first step deposition and (b) the $Cs_{0.15}FA_{0.85}PbI_{3-x}Br_x$ perovskite deposited in three different situations of incomplete drying, optimized drying and optimized drying + LP.

X-ray diffraction patterns of PbI_2-$(FAI)_{0.3}$-$(CsI)_{0.15}$ film after the first step and perovskite films after annealing are shown in **Figures 4 a and b,** respectively. For each step, we took the XRD pattern of both incomplete dried, optimized dried, and optimized dried + LP additive films. According to **Figure 4 a**, the drying condition influences phase formation and crystallinity degree. In incomplete drying, a sharp peak at 12.7 ° indicates the presence of highly crystalline PbI_2 and δ-FAPI peak at 11.9 ° are observable since PbI_2 is partially converted to the δ-FAPI perovskite phase due to FAI reaction with PbI_2. After conversion to perovskite (**figure 4 b**), a substantial amount of PbI_2 and the δ-FAPI phase is still observed. However, in optimized drying, there is no evidence of crystalline FAPI formation in the first step and PbI_2 is fully converted to perovskite phase after annealing, as the 12.7 ° peak is eliminated. In the optimized dried film, PbI2 is less crystalline as indicated with a broader peak with a full-with-half maximum (FWHM) of 0.945 compared to the sharp peak with that of 0.197 for incomplete drying. This implies that less crystalline PbI_2 is more likely to convert to the perovskite phase. The addition of LP does not alter the XRD pattern of the first step deposition. However, after the second step of deposition and annealing, samples with LP additive show better crystallinity and more intense peaks of FAPI and $CsPbI_3$. Furthermore, LP helped to eliminate the elimination of δ-FAPI peak at 11.9 ° and there is no evidence of other major peaks of δ-FAPI [63] The peaks of cubic FAPI and $CsPbI_3$ at 13.9 ° and 13.2 ° are visible in the optimized dried perovskite, which proves the presence of the perovskite phase.
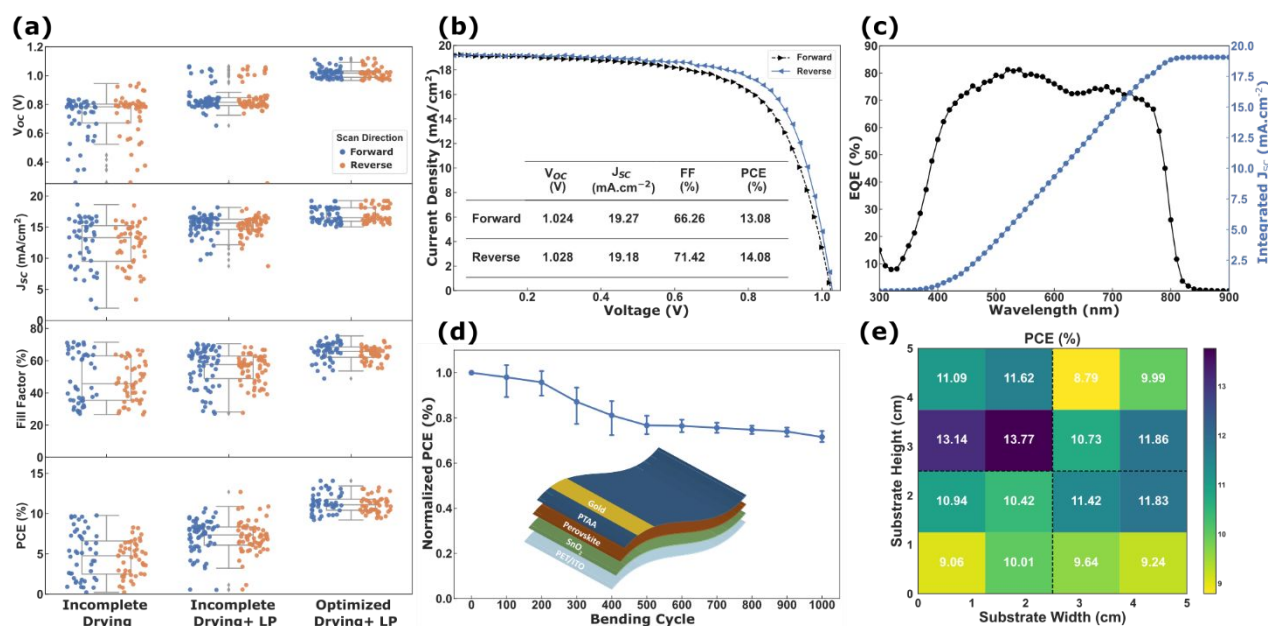
Figure 5. Solar cell characterization (a) box plots of photovoltaic parameters for flexible PSC, in three conditions: incomplete drying, incomplete drying + LP, and optimized drying + LP, obtained from 160 small cells (b and c) J-V curve and IPCE of the champion device, obtained by optimized drying + LP measured under AM 1.5G illumination. (d) The repetitive mechanical bendi7ng test of flex-PSC device and the schematic of device architecture. (e) The distribution of PCE on a 5x5 cm² substrate after cutting and measuring four small-area cells was obtained by optimized drying + LP.

We fabricated flex-PSCs with the perovskite layer deposited via incomplete drying, incomplete drying using LP additive, and optimized drying using LP additive. **Figure 5 (a)** shows the box plot comparing the photovoltaic parameters of these three groups. The incomplete drying cells show the lowest fill factor due to poor morphology and high surface roughness of the perovskite layer, and the maximum efficiency of 9.78% has been obtained. By using the optimized drying technique and the LP additive, the PCE of the champion device was increased to 14.08%. The summary of data is shown in the **Table S2**. The J-V characteristic and the IPCE spectrum of the optimized cell are demonstrated in **Figures 5 b** and **c**. The mechanical stability of flex-PSCs have been investigated by bending the complete device using a cylinder with the radius of 18 mm. The results of this test based on four devices is presented in **Figure 5 d**. On average, the devices maintained 95% performance after 200 bending cycles and 70% after 1000 bending cycles.

 As mentioned in the Experimental Methods section, we used 7×5 cm² substrates for deposition and then cut them to measure small cells. The distribution of the performance of solar cells on one substrate is illustrated in **Figure 5 e**. This proves the uniformly distributed performance of the cells across the bladed substrates. To further investigate the distribution of cells performance across 7×5 cm² substrates, the mean value of normalized PCE for incomplete drying cells and optimized drying + LP cells is mapped in **Figures S6 a** and **b**. It is apparent that in the case of incomplete drying the pattern is arbitrary since the drying occurs in an uncontrolled way. However, in the optimized drying case, a gradient in the performance on the edges of samples is visible which could be due to lamination defects. Next, we also deposited the PTAA layer by blade coating using the same solution used for spin coating. The best-resulted all-blade cell obtained delivered 13.93% PCE with an average PCE of 10.5% across one 7×5 cm²(**Figure S5**).

We transferred the devices to modules with 5×5 cm² and 9.7×9.7 cm² active area to demonstrate the scalability of the optimized fabrication process. Due to the increase in the substrate size and, respectively, the meniscus bar, an adjustment of the precursor solution volume to form the meniscus between the blade and the substrate for all three layers (SnO$_2$, perovskite, and PTAA) is done. The all-bladed flexible modules with a 25 cm² and 94 cm² active area deposited by a sustainable solvent system showed 6.58% and 3.92% PCE respectively as shown in **Figures 6 a** and **b**. This is the largest all-bladed flexible module reported so far, to the best of our knowledge.
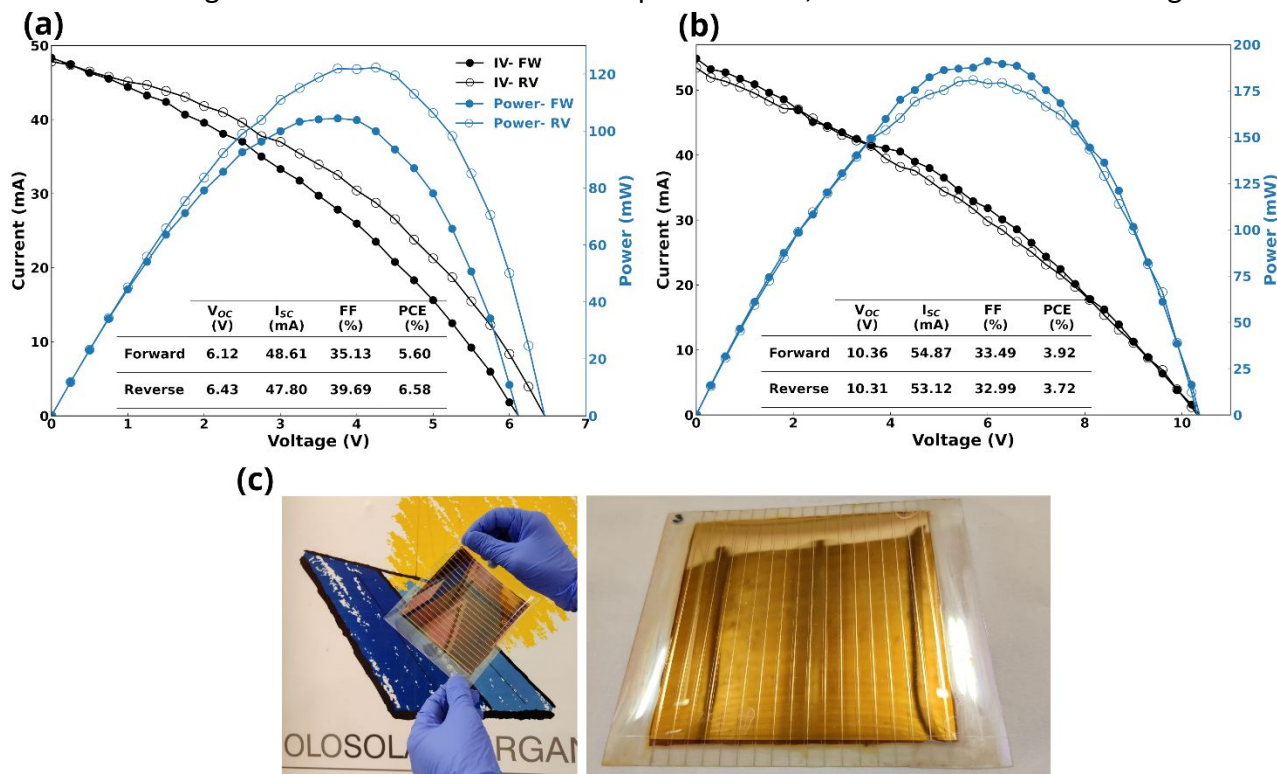

(a)

	V_{OC} (V)	I_{SC} (mA)	FF (%)	PCE (%)
Forward	6.12	48.61	35.13	5.60
Reverse	6.43	47.80	39.69	6.58

(b)

	V_{OC} (V)	I_{SC} (mA)	FF (%)	PCE (%)
Forward	10.36	54.87	33.49	3.92
Reverse	10.31	53.12	32.99	3.72

(c)

Figure 6. I-V curves of (a) 25 cm² module and (b) 94 cm² module. (c). The photographic pictures of the front and back of the 13×13 cm² substrate with 94 cm² aperture area.

Conclusion

In conclusion, all-blade coated flexible perovskite solar cells and modules were fabricated using a sustainable solvent system to avoid the use of toxic solvents such as DMF, NMP, and 2-ME. We showed that high temperature is not required to deposit perovskite in a DMSO-based solvent in ambient air. Double-cation perovskite deposited on a PET substrate by adding nonstoichiometric amounts of FAI/CsI to the PbI$_2$ solution and optimized drying of the blade-coated film using moderate substrate temperature and air knife. The δ-FAPI phase was eliminated, and morphology improved by additive engineering. Champion devices get 14.08% PCE and the process was proven to be transferable to larger substrates up to 13×13 cm². We reported for the first time fully-blade coated and flex-PSM with a 9.7×9.7 cm² (94 cm²) aperture area. Further efforts should be focused on improving the performance of these ambient-air fabricated modules.

Author Contributions

Farshad Jafarzadeh: Conceptualization, Investigation, Visualization, Data Curation, Writing – original draft. **Luigi Angelo Castriotta**: Conceptualization, Investigation, Resources. **Francesca De Rossi:** Conceptualization, Investigation, Project administration, Validation, Writing – review & editing. **Jazib Ali**: Investigation. **Francesco Di Giacomo:** Methodology, Resources. **Aldo Di Carlo:** Supervision. **Fabio Matteocci:** Conceptualization, Project administration, Supervision. **Francesca Brunetti:** Supervision, Project administration, Funding acquisition.

Conflicts of interest
There are no conflicts of interest to declare.

References
1   P. Docampo, J. M. Ball, M. Darwich, G. E. Eperon and H. J. Snaith, *Nat. Commun.*, 2013, **4**, 2761.
2   M. Kaltenbrunner, G. Adam, E. D. Głowacki, M. Drack, R. Schwödiauer, L. Leonat, D. H. Apaydin, H. Groiss, M. C. Scharber, M. S. White, N. S. Sariciftci and S. Bauer, *Nat. Mater.*, 2015, **14**, 1032–1039.
3   E. Leccisi and V. Fthenakis, *Prog. Photovolt. Res. Appl.*, 2021, **29**, 1078–1092.
4   Y. Hu, T. Niu, Y. Liu, Y. Zhou, Y. Xia, C. Ran, Z. Wu, L. Song, P. Müller-Buschbaum, Y. Chen and W. Huang, *ACS Energy Lett.*, 2021, **6**, 2917–2943.
5   P. Kajal, B. Verma, S. G. R. Vadaga and S. Powar, *Glob. Chall.*, 2022, **6**, 2100070.
6   Y. Jiang and Y. Qi, *Mater. Chem. Front.*, 2021, **5**, 4833–4850.
7   L. Li, Y. Wang, X. Wang, R. Lin, X. Luo, Z. Liu, K. Zhou, S. Xiong, Q. Bao, G. Chen, Y. Tian, Y. Deng, K. Xiao, J. Wu, M. I. Saidaminov, H. Lin, C.-Q. Ma, Z. Zhao, Y. Wu, L. Zhang and H. Tan, *Nat. Energy*, , DOI:10.1038/s41560-022-01045-2.
8   V. Romano, A. Agresti, R. Verduci and G. D'Angelo, *ACS Energy Lett.*, 2022, 2490–2514.
9   Z. Wang, X. Zhu, J. Feng, D. Yang and S. (Frank) Liu, *Sol. RRL*, 2021, **5**, 2100264.
10 F. Fu, T. Feurer, T. Jäger, E. Avancini, B. Bissig, S. Yoon, S. Buecheler and A. N. Tiwari, *Nat. Commun.*, 2015, **6**, 8932.
11 K.-L. Wang, Y.-H. Zhou, Y.-H. Lou and Z.-K. Wang, *Chem. Sci.*, 2021, **12**, 11936–11954.
12 C. Teixeira, P. Spinelli, L. A. Castriotta, D. Müller, S. Öz, L. Andrade, A. Mendes, A. D. Carlo, U. Würfel, K. Wojciechowski and D. Forgács, *Adv. Funct. Mater.*, 2022, 2206761.
13 O. Y. Gong, G. S. Han, S. Lee, M. K. Seo, C. Sohn, G. W. Yoon, J. Jang, J. M. Lee, J. H. Choi, D.-K. Lee, S. B. Kang, M. Choi, N.-G. Park, D. H. Kim and H. S. Jung, *ACS Energy Lett.*, 2022, 2893–2903.
14 J. Chung, S. S. Shin, K. Hwang, G. Kim, K. W. Kim, D. S. Lee, W. Kim, B. S. Ma, Y.-K. Kim, T.-S. Kim and J. Seo, *Energy Environ. Sci.*, 2020, **13**, 4854–4861.
15 M. F. Mohamad Noh, N. A. Arzaee, I. N. Nawas Mumthas, N. A. Mohamed, S. N. F. Mohd Nasir, J. Safaei, A. R. bin M. Yusoff, M. K. Nazeeruddin and M. A. Mat Teridi, *J. Mater. Chem. A*, 2020, **8**, 10481–10518.

16 Y. Xiao, C. Zuo, J. Zhong, W. Wu, L. Shen and L. Ding, *Adv. Energy Mater.*, 2021, **11**, 2100378.

17 J. Yan, T. J. Savenije, L. Mazzarella and O. Isabella, *Sustain. Energy Fuels*, 2022, **6**, 243–266.

18 C. Liu, Y.-B. Cheng and Z. Ge, *Chem. Soc. Rev.*, 2020, **49**, 1653–1687.

19 J. Li, R. Munir, Y. Fan, T. Niu, Y. Liu, Y. Zhong, Z. Yang, Y. Tian, B. Liu, J. Sun, D.-M. Smilgies, S. Thoroddsen, A. Amassian, K. Zhao and S. (Frank) Liu, *Joule*, 2018, **2**, 1313–1330.

20 Z. Yang, C.-C. Chueh, F. Zuo, J. H. Kim, P.-W. Liang and A. K.-Y. Jen, *Adv. Energy Mater.*, 2015, **5**, 1500328.

21 Z. Huang, X. Hu, Z. Xing, X. Meng, X. Duan, J. Long, T. Hu, L. Tan and Y. Chen, *J. Phys. Chem. C*, 2020, **124**, 8129–8139.

22 F. Matteocci, L. Vesce, F. U. Kosasih, L. A. Castriotta, S. Cacovich, A. L. Palma, G. Divitini, C. Ducati and A. Di Carlo, *ACS Appl. Mater. Interfaces*, 2019, **11**, 25195–25204.

23 L. A. Castriotta, R. Fuentes Pineda, V. Babu, P. Spinelli, B. Taheri, F. Matteocci, F. Brunetti, K. Wojciechowski and A. Di Carlo, *ACS Appl. Mater. Interfaces*, 2021, **13**, 29576–29584.

24 L. A. Castriotta, F. Matteocci, L. Vesce, L. Cinà, A. Agresti, S. Pescetelli, A. Ronconi, M. Löffler, M. M. Stylianakis, F. Di Giacomo, P. Mariani, M. Stefanelli, E. M. Speller, A. Alfano, B. Paci, A. Generosi, F. Di Fonzo, A. Petrozza, B. Rellinghaus, E. Kymakis and A. Di Carlo, *ACS Appl. Mater. Interfaces*, 2021, **13**, 11741–11754.

25 P. W. Fong, H. Hu, Z. Ren, K. Liu, L. Cui, T. Bi, Q. Liang, Z. Wu, J. Hao and G. Li, *Adv. Sci.*, 2021, **8**, 2003359.

26 H. Wang, Z. Huang, S. Xiao, X. Meng, Z. Xing, L. Rao, C. Gong, R. Wu, T. Hu, L. Tan, X. Hu, S. Zhang and Y. Chen, *J. Mater. Chem. A*, 2021, **9**, 5759–5768.

27 M. Ernst, J.-P. Herterich, C. Margenfeld, M. Kohlstädt and U. Würfel, *Sol. RRL*, 2022, **6**, 2100535.

28 F. Yang, L. Dong, D. Jang, K. C. Tam, K. Zhang, N. Li, F. Guo, C. Li, C. Arrive, M. Bertrand, C. J. Brabec and H. Egelhaaf, *Adv. Energy Mater.*, 2020, **10**, 2001869.

29 Commission Regulation (EU) 2021/2030 of 19 November 2021 amending Annex XVII to Regulation (EC) No 1907/2006 of the European Parliament and of the Council concerning the Registration, Evaluation, Authorisation and Restriction of Chemicals (REACH) as regards N,N-dimethylformamide, https://eur-lex.europa.eu/eli/reg/2021/2030/oj, (accessed August 23, 2022).

30 R. Vidal, J.-A. Alberola-Borràs, S. N. Habisreutinger, J.-L. Gimeno-Molina, D. T. Moore, T. H. Schloemer, I. Mora-Seró, J. J. Berry and J. M. Luther, *Nat. Sustain.*, 2021, **4**, 277–285.

31 J. J. Wu, M. Muruganandham and S. H. Chen, *J. Hazard. Mater.*, 2007, **149**, 218–225.

32 V. Gutmann, *The Donor-Acceptor approach to molecular interactions*, Plenum Press, New York, 1978.

33 J. C. Hamill, J. Schwartz and Y.-L. Loo, *ACS Energy Lett.*, 2018, **3**, 92–97.

34 Y. Deng, C. H. Van Brackle, X. Dai, J. Zhao, B. Chen and J. Huang, *Sci. Adv.*, 2019, **5**, eaax7537.

35 A. A. Petrov, A. A. Ordinartsev, S. A. Fateev, E. A. Goodilin and A. B. Tarasov, *Molecules*, 2021, **26**, 7541.

36 J. Küffner, J. Hanisch, T. Wahl, J. Zillner, E. Ahlswede and M. Powalla, *ACS Appl. Energy Mater.*, 2021, **4**, 11700–11710.

37 N.-G. Park, *Nat. Sustain.*, 2020, **4**, 192–193.

38 S.-H. Huang, K.-Y. Tian, H.-C. Huang, C.-F. Li, W.-C. Chu, K.-M. Lee, Y.-C. Huang and W.-F. Su, *ACS Appl. Mater. Interfaces*, 2020, **12**, 26041–26049.

39 M.-C. Tang, Y. Fan, D. Barrit, X. Chang, H. X. Dang, R. Li, K. Wang, D.-M. Smilgies, S. (Frank) Liu, S. De Wolf, T. D. Anthopoulos, K. Zhao and A. Amassian, *J. Mater. Chem. A*, 2020, **8**, 1095–1104.

40 Y. Fan, J. Fang, X. Chang, M.-C. Tang, D. Barrit, Z. Xu, Z. Jiang, J. Wen, H. Zhao, T. Niu, D.-M. Smilgies, S. Jin, Z. Liu, E. Q. Li, A. Amassian, S. (Frank) Liu and K. Zhao, *Joule*, 2019, **3**, 2485–2502.

41 J. Yang, E. L. Lim, L. Tan and Z. Wei, *Adv. Energy Mater.*, 2022, **12**, 2200975.

42 Y. Zheng, X. Xu, S. Liu, G. Xu, Z. Bi, Y. Zhu, K. Wang, S. (Frank) Liu, A. Guerrero and G. Xing, *Sol. RRL*, 2022, 2200737.

43 F. Di Giacomo, L. A. Castriotta, F. U. Kosasih, D. Di Girolamo, C. Ducati and A. Di Carlo, *Micromachines*, 2020, **11**, 1127.

44 D. A. Lange, H. M. Jennings and S. P. Shah, *J. Mater. Sci.*, 1993, **28**, 3879–3884.

45 A. Mínguez-Martínez, P. Maresca, J. Caja and J. de V. y Oliva, *Materials*, 2022, **15**, 5495.

46 D. Nečas and P. Klapetek, *Open Phys.*, , DOI:10.2478/s11534-011-0096-2.

47 D. Prat, A. Wells, J. Hayler, H. Sneddon, C. R. McElroy, S. Abou-Shehada and P. J. Dunn, *Green Chem.*, 2016, **18**, 288–296.

48 V. Zardetto, T. M. Brown, A. Reale and A. Di Carlo, *J. Polym. Sci. Part B Polym. Phys.*, 2011, **49**, 638–648.

49 In *Handbook of Nucleating Agents*, Elsevier, 2016, pp. 1–3.

50 X. Xu, C. Ma, Y.-M. Xie, Y. Cheng, Y. Tian, M. Li, Y. Ma, C.-S. Lee and S.-W. Tsang, *J. Mater. Chem. A*, 2018, **6**, 7731–7740.

51 B. Dou, J. B. Whitaker, K. Bruening, D. T. Moore, L. M. Wheeler, J. Ryter, N. J. Breslin, J. J. Berry, S. M. Garner, F. S. Barnes, S. E. Shaheen, C. J. Tassone, K. Zhu and M. F. A. M. van Hest, *ACS Energy Lett.*, 2018, **3**, 2558–2565.

52 Y. Fan, J. Fang, X. Chang, M.-C. Tang, D. Barrit, Z. Xu, Z. Jiang, J. Wen, H. Zhao, T. Niu, D.-M. Smilgies, S. Jin, Z. Liu, E. Q. Li, A. Amassian, S. (Frank) Liu and K. Zhao, *Joule*, 2019, **3**, 2485–2502.

53 S.-H. Huang, K.-Y. Tian, H.-C. Huang, C.-F. Li, W.-C. Chu, K.-M. Lee, Y.-C. Huang and W.-F. Su, *ACS Appl. Mater. Interfaces*, 2020, **12**, 26041–26049.

54 S. Chen, X. Xiao, H. Gu and J. Huang, *Sci. Adv.*, 2021, **7**, eabe8130.

55 Y. Deng, C. H. Van Brackle, X. Dai, J. Zhao, B. Chen and J. Huang, *Sci. Adv.*, 2019, **5**, eaax7537.

56 K. W. Lau, M.-H. H. Aron, M. H.-J. Yen, E. Y. Fung, S. Grzybicki, R. Matamoros and J. C. Curtis, *Inorganica Chim. Acta*, 1994, **226**, 137–143.

57 W. Linert, R. F. Jameson and A. Taha, *J Chem Soc Dalton Trans*, 1993, 3181–3186.

58 J. Li, J. Dagar, O. Shargaieva, M. A. Flatken, H. Köbler, M. Fenske, C. Schultz, B. Stegemann, J. Just, D. M. Többens, A. Abate, R. Munir and E. Unger, *Adv. Energy Mater.*, 2021, **11**, 2003460.

59 S. Chen, X. Xiao, H. Gu and J. Huang, *Sci. Adv.*, 2021, **7**, eabe8130.

60 X. Zheng, B. Chen, J. Dai, Y. Fang, Y. Bai, Y. Lin, H. Wei, X. C. Zeng and J. Huang, *Nat. Energy*, 2017, **2**, 17102.

61 Y. Deng, X. Zheng, Y. Bai, Q. Wang, J. Zhao and J. Huang, *Nat. Energy*, 2018, **3**, 560–566.

62 N.-G. Park and K. Zhu, *Nat. Rev. Mater.*, 2020, **5**, 333–350.

63 M. P. U. Haris, S. Kazim and S. Ahmad, *ACS Appl. Mater. Interfaces*, 2022, **14**, 24546–24556.